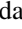
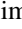





Kindling the First Stars. I. Dependence of Detectability of the First Stars with JWST on the Population III Stellar Masses

Mia Sauda Bovill¹, Massimo Stiavelli² , Alessa Ibrahim Wiggins³, Massimo Ricotti¹ , and Michele Trenti^{4,5} 

¹ Department of Astronomy, University of Maryland, College Park, College Park, MD, USA

² Space Telescope Science Institute, 3700 San Martin Drive, Baltimore, MD, USA

³ Department of Physics and Astronomy, Texas Christian University, Fort Worth, TX, USA

⁴ School of Physics, University of Melbourne, Parkville 3010, VIC, Australia

⁵ ARC Centre of Excellence for All Sky Astrophysics in 3 Dimensions (ASTRO 3D), Australia

Received 2022 August 25; revised 2023 December 2; accepted 2023 December 10; published 2024 February 6

Abstract

The first Population III (Pop III) stars formed out of primordial, metal-free gas, in minihalos at $z > 20$, and kickstarted the cosmic processes of reionization and enrichment. While these stars are likely more massive than their enriched counterparts, the current unknowns of their astrophysics include when the first Pop III stars ignited, how massive they were, and when and how the era of the first stars ended. Investigating these questions requires an exploration of a multidimensional parameter space, including the slope of the Pop III stellar initial mass function (IMF) and the strength of the nonionizing UV background. In this work, we present a novel model which treats both the slope and maximum mass of Pop III stars as truly free parameters while including the physics of the fragmentation of primordial gas. Our results also hint at a nonuniversal Pop III IMF which is dependent on the efficiency of primordial gas fragmentation. Our relatively simple model reproduces the results from hydrodynamic simulations, but with a computational efficiency which allows us to investigate the observable differences between a wide range of potential Pop III IMFs. In addition, the evolution of the number density of Pop III stars may provide insight into the evolution of the H_2 dissociating background. While the slope of the Pop III IMF does not significantly affect the predicted number density of the first stars, more top-heavy IMFs produce Pop III star clusters which are 2–3 magnitudes brighter than their more bottom-heavy counterparts. While the Pop III star clusters are too dim for direct detection by JWST, we find they are within the reach of gravitational lensing.

Unified Astronomy Thesaurus concepts: [Population III stars \(1285\)](#); [N-body simulations \(1083\)](#); [Theoretical models \(2107\)](#)

1. Introduction

The first population of stars which formed out of material with primordial chemical composition are commonly referred to as Population III (Pop III) stars. In Lambda cold dark matter (Λ CDM), the first stars form in minihalos at $z > 30$ (Abel et al. 2002). Understanding the astrophysical nature of Pop III stars is of fundamental importance, as they begin the process of reionization and the enrichment of the intergalactic medium (IGM), paving the way for the first Population II (Pop II) galaxies. With the successful launch of JWST, we stand on the precipice of an unprecedented era in the study of the first stars; however, basic questions of the physical properties Pop III stars remain.

While there is consensus that the typical Pop III star is more massive than their enriched Pop II or Population I counterparts, the actual mass distribution of Pop III stars remains unknown. Some work suggests masses $>200 M_{\odot}$ (Bromm et al. 1999; Abel et al. 2000) with an upper limit of $1000 M_{\odot}$ (Ohkubo et al. 2009) or higher (Haemmerlé et al. 2021). Other theoretical studies suggest that Pop III stars could have a wide range of masses possibly extending down to solar masses and below (Yoshida et al. 2006; Clark et al. 2011; Greif et al. 2011; Susa 2013; Stacy et al. 2016; Sugimura et al. 2020; Wollenberg et al. 2020; Park et al. 2021a, 2021b; Latif et al. 2022; Prole

et al. 2022). As such, we do not have an understanding of either the shape of the Pop III stellar initial mass function (IMF) *nor* the maximum mass for a Pop III star. Both the formation and evolution of these objects are likely different from that of enriched stars in the local Universe and are currently observationally unconstrained.

One possibility for the study of Pop III stars is to look at ultra-metal-poor stars in the local Universe. If Pop III stars formed at sufficiently low masses, some may have survived to $z = 0$ (Dutta et al. 2020). However, such a detection has not yet occurred and may be complicated by environmental effects such as pollution of the photosphere by supernova ejecta (Suda et al. 2021). It is unclear whether this implies that low-mass ($<1 M_{\odot}$) Pop III stars did not form, have been polluted, or are simply too rare. Alternatively, one could attempt to detect the chemical signatures of nucleosynthesis in, and supernovae of, Pop III stars in the next generation of stars; however, it is unclear whether such signatures would be recognizable (Sarmiento et al. 2017; Chiaki & Wise 2019; Jeon et al. 2021).

The second possibility is to detect Pop III stars or their supernovae at $z > 6$. Direct detection of Pop III stars or star clusters is unlikely as the number densities are too low for detection with JWST (Rydberg et al. 2013). Even the tentative identification of the CR7 source with a Pop III object is now mostly discounted (Sobral et al. 2015). However, detection with the aid of gravitational lensing is more promising and has been investigated for magnifications of known lensing clusters (Zackrisson et al. 2015; Windhorst et al. 2018). Detection of

Table 1
Simulations

Simulation	L (Mpc h ⁻¹ comoving)	N
2M_512	2	512
4M_1024	4	1024

Pop III stars via gravitational lensing requires detailed lensing models, which exist for a variety of lensing clusters (Lam et al. 2014; Jauzac et al. 2015a, 2015b; Diego et al. 2015, 2016). In addition, individual stars magnified by an order of 10,000 have been detected in caustics (Vanzella et al. 2020; Welch et al. 2022) and evidence exists that these high-redshift stars are $>50 M_{\odot}$ (Welch et al. 2022).

A fraction of Pop III stars end their lives as pair-instability supernovae (PISNe). These supernovae require high masses (140–260 M_{\odot}) and have 100 times the energy of their core-collapse counterparts. As such, PISNe are expected to be extremely luminous and would easily be above the detectability threshold for JWST (Whalen et al. 2013, 2014; Moriya et al. 2022), assuming their rate is high enough (Lazar & Bromm 2022).

While both detection via gravitational lensing and PISNe are within reach of JWST, determining the astrophysics of the underlying population requires a comparison with theoretical simulations and models of the first stars. Hydrodynamical simulations have now reached the parsec resolutions required to study the first stars in a cosmological context (Wise et al. 2012; Xu et al. 2016). However, while some studies have explored the implications for a range of Pop III IMFs (Lazar & Bromm 2022), computational expense means most cosmological simulations of the first billion years assume a single power-law IMF with an exponential cutoff (Skinner & Wise 2020). Given the unconstrained nature of the Pop III IMF, a full exploration of parameter space is required for the upcoming observations to inform the astrophysics underlying the formation of the first stars.

In this work, we introduce a new semi-analytic model and present the new results on the detectability of the first stars with JWST for a range of assumptions for the Pop III IMFs and the maximum Pop III mass. We describe our simulations in Section 2 and the how the relevant physics is implemented in our model in Section 2.1. Results are given in Section 3, and the implications for detection of Pop III stars with JWST are discussed in Section 4.

2. Simulations

In this section, we describe the numerical simulations and modeling presented in this work. We have generated initial conditions for a set of two high-resolution simulations using WMAP9 cosmology ($\Omega_M = 0.279$, $\Omega_{\Lambda} = 0.721$, $h_o = 0.7$; Bennett et al. 2013) with MUSIC (Hahn & Abel 2011). The simulations were run with Gadget 2 (Springel 2005) from $z = 150$ to $z = 6$ and analyzed with AMIGA Halo Finder (AHF; Gill et al. 2004; Knollmann & Knebe 2009) and Consistent Trees (Behroozi et al. 2013). The resolution was chosen to resolve all potential sites of Pop III star formation ($M > 10^5 M_{\odot}$) with at least 100 particles. While test runs were done on the Ultra-Deep Field cluster at STScI, both high-

resolution boxes in Table 1 were run and analyzed on the University of Maryland HPC Deepthought2.

2.1. Model

In this section, we describe a novel semi-analytic model which will allow us to investigate the unexplored parameter space of the formation, properties and fates of Pop III stars. Critical physics incorporated into our model includes a variable Pop III IMF, limits for the fragmentation of primordial gas, an external and self-consistent Lyman–Werner (LW) background, and a model for the enrichment of the Pop III host halos and the nearby IGM by supernova.

2.1.1. Mass Thresholds for Pop III Star Formation

The primary driver of whether a given halo will be able to form stars is the strength of the LW background and is determined by four mass thresholds. Here, we provide the analytical forms of those thresholds for the WMAP9 cosmology used in this work. Throughout, we assume a halo is pristine if $Z < 10^{-5} Z_{\odot}$. In the absence of a dissociative UV or X-ray background, a dark-matter halo must simultaneously meet the criteria for H_2 cooling and Jeans’ collapse to be massive enough for its gas to cool and collapse (Tegmark et al. 1997). This gives us

$$M_{\text{vir}}^{\text{III}} = \max \begin{cases} M_{\text{H}_2} = 1.905 \times 10^5 M_{\odot} \left(\frac{1+z}{31} \right)^{-1.5} \\ M_J = 1.36 \times 10^5 M_{\odot} \left(\frac{1+z}{31} \right)^{-2.071} \end{cases}, \quad (1)$$

where $M_{\text{vir}}^{\text{III}}$ is the minimum halo mass required for Pop III star formation at a given redshift without a dissociative background, z . Note, $M_{\text{vir}}^{\text{III}}$ is determined by the Jeans’ collapse, M_J at lower redshift ($z < 16.2$), and by the threshold for H_2 cooling, M_{H_2} at higher redshift ($z > 16.2$).

Before discussing the mass threshold for the LW background, we note that, regardless of the strength of the LW background, a halo above the HI cooling limit, M_{HI} , will be able to cool its pristine gas via the HI pathway:

$$M_{\text{HI}} = 7.75 \times 10^6 M_{\odot} \left(\frac{1+z}{31} \right)^{1.5}, \quad (2)$$

where M_{HI} is the HI cooling mass at a given redshift, z . In addition to being able to cool via neutral hydrogen, halos with $M > M_{\text{HI}}$ will be able to self-shield H_2 , even in the presence of the LW background.

2.1.2. Lyman–Werner Background

Before Pop III stars explode, enriching their host halos and surrounding IGM with metals, they emit nonionizing UV radiation which builds up to form the LW background. As LW photons have a mean free path of approximately 150th of the cosmic horizon (Ricotti et al. 2000; Ricotti 2016), corresponding to ~ 4 Mpc *physical* at $z \sim 10$ (Glover & Brand 2001; Stiavelli 2009), more than 10 times the size of our simulation box, we include an externally generated LW background in our model.

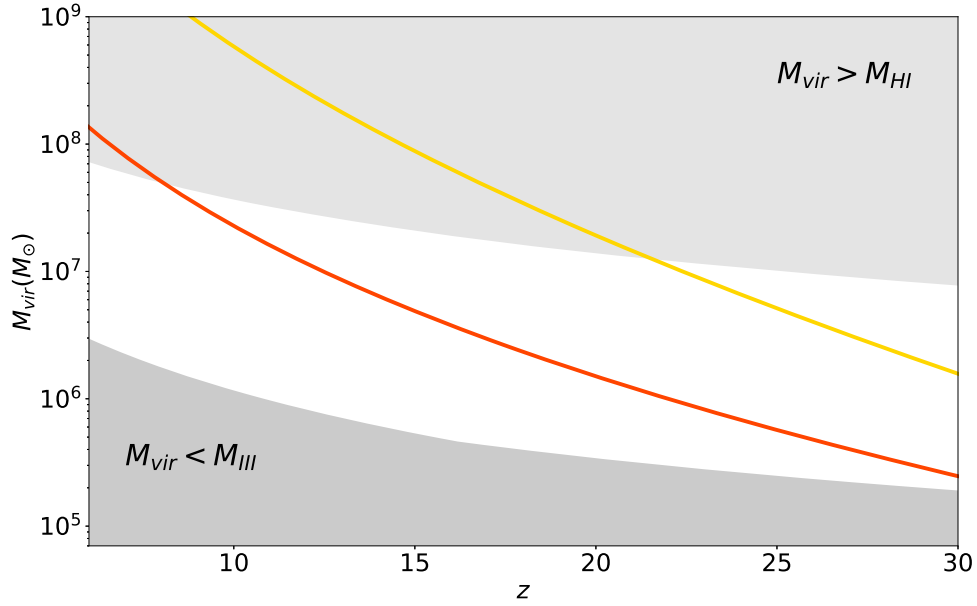


Figure 1. Halo virial mass vs. redshift for various thresholds for Pop III star formation. The dark gray area on the bottom shows the region where a halo will not be able to form Pop III stars because there is either not enough gas to become Jeans unstable or enough H_2 to cool the gas (Equation (1)). The pale gray shaded area at the top is where Pop III stars will always be able to form since $M_{\text{vir}} > M_{\text{HI}}$ and there is sufficient gas to self-shield the H_2 from the LW background. The color lines show the mass thresholds for Pop III star formation for a strong (gold) and weaker (red) LW background from TS09 (Equation (3)).

For a given LW intensity, J_{21} , the minimum mass required for a halo to form Pop III stars is given by

$$M_{\text{LW}} = 6.44 \times 10^6 M_{\odot} J_{21}^{0.457} \left(\frac{1+z}{31} \right)^{-3.557}, \quad (3)$$

where M_{LW} is the mass threshold required for Pop III star formation in the presence of a LW background with intensity J_{21} at a redshift z .

The $M_{\text{LW}}(z)$ dependence for a range of J_{21} values are taken from a subset of the $J_{21}(z)$ models from TS09 (Figure 1). We select the TS09 model by sorting the full range of models into three groups based on the strength of the $J_{21}(z)$. Of the seven cases with a LW background, four (standard Pop III model with a Sheth–Tormen or a Press–Schechter halo mass function and multiple Pop III stars per halo with $\epsilon_{\text{PopIII}} = 0.005$) have a medium-LW background. A reduced f_{esc} produces the one low-LW background case, and the two high-LW cases have a strong external J_{21} field and multiple Pop III stars forming with $\epsilon = 0.05$, respectively.

In this work, we consider the low- and high-LW background cases (Figure 1). While the modeling of the Pop III population in TS09 is different from our model, the low-LW case is roughly consistent with the LW background generated by the stellar populations in our simulations. We have included the strong-LW case to investigate how Pop III star formation would change near an overdense region capable of generating such a background.

Note, $J_{21} = J_{21}^{\text{external}} + J_{21}^{\text{consistent}}$, including both the external LW backgrounds from Trenti & Stiavelli (2009, J_{21}^{external}) and a self-consistent component generated by all Pop III stars and Pop II stars $> 8 M_{\odot}$ ($J_{21}^{\text{consistent}}$). For details of the $J_{21}^{\text{consistent}}$ calculation, see Trenti & Stiavelli (2009).

2.1.3. Pop III Initial Mass Function

In this work, we assume the Pop III IMF is described by a power law. However, we consider the slope of the power law to

be a free parameter. For the IMF slope, we explore $\alpha = [0.2, 0.5, 0.8, 1.0, 1.2, 1.5, 1.8, 2.1, 2.35]$ (Figure 2), where

$$dm/dN = Am^{-\alpha}, \quad (4)$$

where m is the mass of a Pop III star, α is the assumed slope of the Pop III IMF, and A is the normalization for the mass of gas available in the halo.

For all IMF slopes we assume a minimum Pop III mass of $10 M_{\odot}$ and a maximum mass of $1000 M_{\odot}$. In any given halo, the number of Pop III stars which can be formed is set by the maximum mass of Pop III stars, $M_{\text{III}}^{\text{max}}$, and the physics of the fragmentation of primordial gas. The former is given by $M_{\text{III}}^{\text{max}} = \epsilon_{\text{III}}^{\text{max}} f_b M_{\text{vir}}$, where M_{vir} is the virial mass of the halo, f_b is the baryon fraction, and $\epsilon_{\text{III}}^{\text{max}}$ is the maximum possible Pop III star formation efficiency, a parameter provided for the model. Our fiducial value is $\epsilon_{\text{III}}^{\text{max}} = 0.01$.

The latter quantity is calculated with the assumption that the lack of an efficient coolant means primordial gas will not fragment as effectively as enriched gas. An estimate for the maximum number of fragments per halo with M_{vir} at a given redshift z can be derived from Jeans collapse. In order for gas to cool, collapse, and form stars, the total gas mass $M_g > M_J$. We assume the initial temperature of the gas is T_{vir} and the gas cools to a final temperature T_f . If we assume all of the gas in the halo collapses into a single fragment, we recover the Jeans mass requirement for Pop III star formation given in Equation (1); however, this is only true if the gravitational collapse timescale, τ_{coll} , is less than the cooling timescale, τ_{cool} . For massive enough halos $\tau_{\text{coll}} > \tau_{\text{cool}}$, which means the gas cools faster than it collapses, potentially resulting in additional fragmentation (Stiavelli 2009).

To determine the maximum amount of gas fragmentation in a pristine halo with a given M_{vir} at a given redshift z , we start with the simple idea that

$$NM_J \leq M_g = f_b M_{\text{vir}}, \quad (5)$$

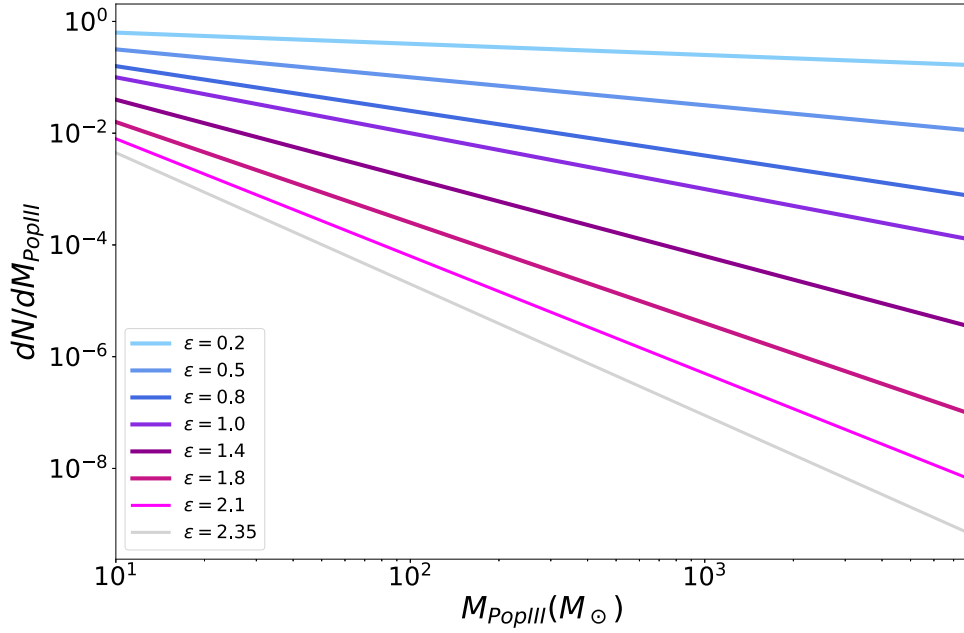


Figure 2. The range of slopes for the Pop III IMF considered in this work. The color-coding in this figure will be used throughout this work for the various IMF slopes.

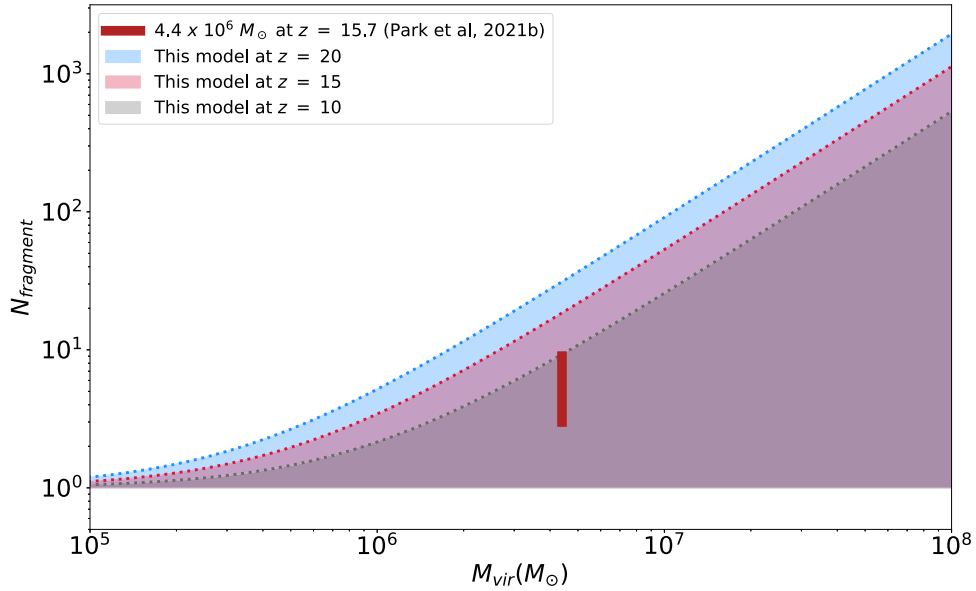


Figure 3. The shaded regions show the number of fragments in a pristine halo as a function of virial mass. The upper edge of the shaded regions is given by Equation (8) for $z = 20$ (blue), $z = 15$ (red), and $z = 10$ (dark gray), and the lower bound by $N_{\text{frag}} = 1$, where $M_J = f_b M_{\text{vir}}$. The dark red bar shows the range of fragmentation for a $4.4 \times 10^6 M_{\odot}$ halo at $z = 15.7$ from Park et al. (2021b).

where N is the maximum number of fragments, M_g is the available gas mass, f_b is the cosmic baryon fraction, and

$$M_J = 8.4 \times 10^6 \left(\frac{M_{\text{vir}}}{10^6 M_{\odot}} \right) \left(\frac{T_f}{T_o} \right)^2, \quad (6)$$

where M_J is the Jeans mass, M_{vir} is the virial mass of a halo, $T_o \approx T_{\text{vir}}$ is the initial temperature of the gas, and T_f is the final temperature of the gas.

Assuming the fraction of baryons in the halos is equal to the cosmic baryon fraction, for the gas to become Jeans unstable ($M_J < M_b$), the gas must cool until $T_{\text{vir}}/T \geq 6.97$. When this is

combined with Equations (5) and (6), this gives us

$$\left(\frac{T_o}{T_f} \right)^2 \geq \frac{f_b}{8.4} N = 6.97^2 N. \quad (7)$$

Given that $T_o = T_{\text{vir}}$ and $T_f \approx 120$ K, the minimum temperature to which H_2 can cool gas (Abel et al. 2000), we have

$$N_{\text{frag}} \leq 9.12 \left(\frac{M_{\text{vir}}}{10^6 M_{\odot}} \right)^{4/3} \left(\frac{1+z}{31} \right)^2, \quad (8)$$

where N_{frag} is the maximum fragmentation of primordial gas in a halo of M_{vir} at a redshift z . The expected number of fragments

for a pristine halo in our model for a given mass at three redshifts is shown in Figure 3. We find our model is consistent with the amount of fragmentation seen in high-resolution hydrodynamical simulations (Park et al. 2021b).

Physically, this means a halo of M_{vir} at a redshift z will have primordial gas fragmentation into $< N_{\text{frag}}$ fragments. However, multiple Pop III stars may form per fragment, as high-resolution hydrodynamic simulations suggest as many as six Pop III stars can form per fragment (Susa et al. 2014). In our model, this is parameterized as a constraint on the maximum number of Pop III stars N_{III} , where $N_{\text{frag}} < N_{\text{III}} > 6N_{\text{frag}}$.

We find that for a given $\epsilon_{\text{III}}^{\text{max}}$, N_{frag} decreases for all Pop III IMFs and the effect is larger for the more top-heavy Pop III IMFs. In addition, we find that as the average number of stars per fragment increases, N_{frag} decreases regardless of the choice of $\epsilon_{\text{III}}^{\text{max}}$ and the Pop III IMF, however the effect is greater for more top-heavy Pop III IMFs and lower $\epsilon_{\text{III}}^{\text{max}}$.

The explanation for both trends is in the combination of two effects. First, it is important to note that Equation (8) gives a maximum number of fragments for a primordial halo with M_{vir} at a given redshift. Our model allows the primordial gas to fragment less than this limit. Second, that the total mass of Pop III stars in any halo, M_{III} , is limited to $M_{\text{III}} \leq \epsilon_{\text{III}}^{\text{max}} f_b M_{\text{vir}}$. In this work, a Pop III star-forming halo must meet both criteria. Therefore, lower values of $\epsilon_{\text{III}}^{\text{max}}$ limit the total mass budget available for Pop III stars, and more top-heavy Pop III IMFs place more of that mass budget into fewer, more massive stars. The more stars that form in a typical fragment, the less gas fragmentation is required before the mass budget for Pop III stars is exceeded.

For the power-law IMF we randomly sample the power law with $m_{\text{min}} = 10 M_{\odot}$. The power law is resampled until a distribution of masses is produced for which $M_{\text{tot}} \leq M_{\text{PopIII}}$ and $N_{\text{tot}} \leq N_{\text{III}} N_{\text{frag}}$. For the Pop III IMF power-law slopes, when both the mass of the gas reservoir and the fragmentation of the primordial gas are taken into account, our results become insensitive to the choice of a Pop III star formation efficiency. We define the de facto Pop III star formation efficiency as $M_{\text{PopIII}}/f_b M_{\text{vir}}$.

As seen in Figure 4, the de facto Pop III star formation efficiencies from our relatively simple model are in reasonable agreement with Pop III star formation efficiencies measured in high-resolution hydrodynamic simulations of the first stars (Skinner & Wise 2020).

Figure 4 shows that for bottom-heavy IMFs, the measured Pop III star formation efficiency is independent of our choice of ϵ_{III} . This is due to the limited fragmentation of the primordial gas, which places an upper limit on the number of Pop III stars that can form. For the more top-heavy IMFs, our choice of ϵ_{III} does affect the de facto star formation efficiency. At $z > 20$, there is increasing scatter in the de facto Pop III star formation efficiency with an increasingly top-heavy IMF. This is likely driven by the stochastic population of the high-mass end of the IMF. This suggests that the efficiency of the fragmentation of primordial gas is a significant driver of the Pop III IMF. The more efficient the fragmentation, the more bottom heavy the IMF. The fragmentation of primordial gas can be increased by turbulence and torques from nearby halos. As both of these effects increase with decreasing redshift, the changing

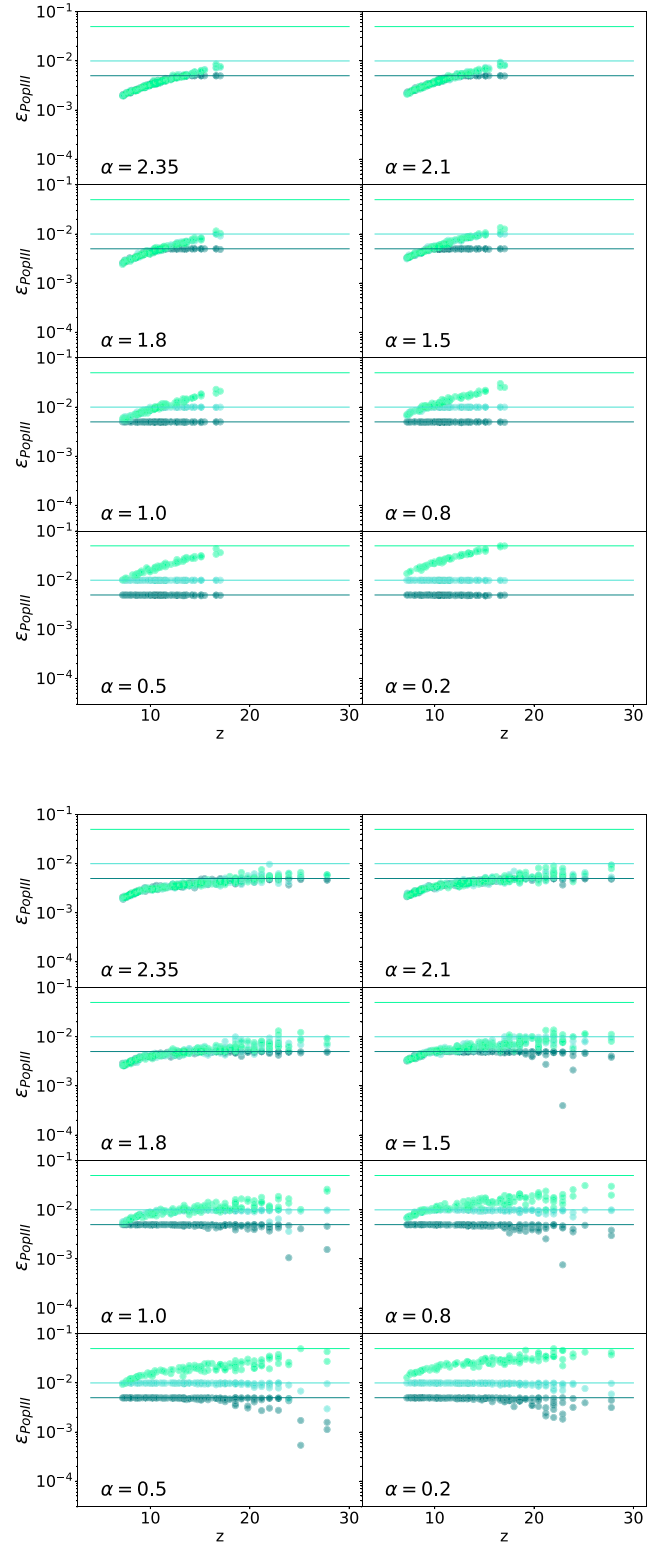


Figure 4. The actual efficiency of Pop III star formation, defined as $\epsilon_{\text{PopIII}} = M_{\text{III}}/f_b M_{\text{vir}}$ for our range of Pop III IMF slopes (Figure 2) and the low (lower) and high (upper) external LW backgrounds (Figure 1) for three values of $\epsilon_{\text{III}} = [0.005(\text{dark blue}), 0.01(\text{turquoise}), 0.05(\text{green})]$ inputted into the model. Note that for the bottom-heavy IMFs, ϵ_{PopIII} is independent of the value of ϵ_{III} inputted into the model.

fragmentation of primordial gas with redshift may result in a nonuniversal Pop III IMF which evolves with both halo mass and redshift.

2.1.4. Metal Enrichment

To determine when the transition from unenriched to enriched star formation occurred, we must determine when and where there has been metal enrichment. The metal enrichment due to the first stars is driven by the fates of the first stars. In our model this is given by

$$\begin{cases} m < 140 M_{\odot} & \text{CCSN} \\ 140 M_{\odot} < m < 260 M_{\odot} & \text{PISN} \\ 260 M_{\odot} < m & \text{DCBH} \end{cases}, \quad (9)$$

from Heger et al. (2003). For Pop III stars which die as direct-collapse black holes (DCBHs), we assume the host halo has been enriched, but that any metal enrichment remained trapped in the host halo and did not enrich the surrounding IGM. For enrichment by Pop III stars which die by core-collapse supernovae (CCSNe) and PISNe, we use the prescription discussed below.

The Pop III era is ended by enrichment of halos and the IGM by the first supernovae. In order for a halo to form Pop III stars its gas must have $Z < Z_{\text{crit}}$. We assume a $Z_{\text{crit}} \approx -5$, however our results are not sensitive to this choice.

For a halo to be considered pristine ($Z < Z_{\text{crit}}$) in our model it must meet two criteria: no progenitor halo has formed either Pop III or Pop II stars, and no progenitor halo was polluted by supernova ejecta from a neighboring halo. Determining the latter criteria requires a simple model to determine whether the supernova ejecta have enough mechanical energy, E_{SN} , to leave the halo and how far into the IGM the ejecta spread if they do. Supernova ejecta are contained within the host halo if

$$M_{\text{contain}} = 7.96 \times 10^6 M_{\odot} \left(\frac{E_{\text{SN}}}{10^{51} \text{ erg}} \right)^{3/5} \left(\frac{1+z}{31} \right)^{-3/5}, \quad (10)$$

where E_{SN} is the amount of kinetic energy energy generated by Pop III supernovae, $f_{\text{kin}} (10^{51} \text{ erg} N_{\text{CCSN}} + 10^{53} \text{ erg} N_{\text{PISN}})$, in a halo with M_{vir} at a redshift z . In our fiducial model we assume $f_{\text{kin}} = 30\%$ of the SN energy is converted into mechanical energy. In our model we assume all supernova from a given burst of star formation have at roughly the same time exploded and ejecta have dispersed within the 10 Myr before the next simulation snapshot. If $M_{\text{vir}} \geq M_{\text{contain}}$, then we assume the enriched supernova ejecta remain confined to the halo and do not pollute the surrounding IGM, while if $M_{\text{vir}} < M_{\text{contain}}$ then a fraction of the enriched supernova ejecta escapes from the parent halo and pollutes the surrounding IGM.

In the latter case, we can use physical arguments to estimate the radius of the enriched ejecta, R_{ej} . Outside of the initial halo, we assume a constant IGM density, ρ_{IGM} , where ρ_{IGM} is simply the mass density of nonvirialized mass at a redshift z . Given that the physical IGM in the immediate vicinity of a halo is clumpier and denser than these assumptions, the R_{ej} we calculate can be seen as an upper bound on the results of a more complex treatment.

For the mass enclosed inside the ejecta radius, we assume the enriched gas expands until the thermal speed of the gas is equal to the escape speed from the halo:

$$v_{\text{esc}}^2 = v_{\text{th}}^2 = \frac{2E_{\text{SN}}}{3f_b M(<R_{\text{ej}})}, \quad (11)$$

where E_{SN} is the mechanical energy of supernovae from a halo, f_b is the baryon fraction, $M(<R_{\text{ej}})$ is the mass enclosed within the host halo and a smooth IGM with $r < R_{\text{ej}}$, v_{esc} is the escape velocity at R_{ej} , and v_{th} is the thermal speed given by E_{SN} . This gives us

$$\frac{E_{\text{SN}}}{3f_b G} = \frac{M^2(<R_{\text{ej}})}{R_{\text{ej}}}. \quad (12)$$

For our assumption of a smooth IGM, we can write $M(<R_{\text{ej}}) = M_{\text{vir}} + \frac{4\pi}{3} \rho_{\text{IGM}} (R_{\text{ej}}^3 - R_{\text{vir}}^3)$, where $\rho_{\text{IGM}} = (1 - f_{\text{coll}}(z)) \rho_b (1+z)^3$, $M_{\text{vir}} = \frac{4\pi}{3} \xi_{\text{vir}} R_{\text{vir}}^3$, and $\xi_{\text{vir}} \sim 178 \rho_b (1+z)^3$. Combining these with Equation (11) gives

$$\frac{E_{\text{SN}}}{f_b G} = \frac{\left(M_{\text{vir}} + \frac{4\pi}{3} \rho_{\text{IGM}}(z) (R_{\text{ej}}^3 - R_{\text{vir}}^3) \right)^2}{R_{\text{ej}}}, \quad (13)$$

where E_{SN} is the energy of a supernova in a halo of M_{vir} and R_{vir} at a redshift z expanding into a smooth IGM.

3. Results

3.1. Lyman–Werner Background

We first look at when and in what halos Pop III stars formed. Figure 5 shows the virial mass versus redshift of the dark-matter halos which formed Pop III stars for the full range of the Pop III IMF slopes and LW backgrounds considered in this work. As expected, the redshift at which Pop III stars form decreases as the strength of the LW background increases. Concurrently, the typical mass of halos forming Pop III stars increases as the strength of the LW background increases. This is due to the increased suppression of star formation in low-mass halos. For detectability, the best option is Pop III stars forming at $z < 15$ in halos above the atomic cooling limit. As seen in Figure 5, these atomic cooling Pop III halos are present for all external LW backgrounds and Pop III IMFs explored in this work.

While variations in the number density of Pop III stars forming halos is secondary to the differences driven by the strength of the LW background, we do observe trends. We note that as the Pop III IMF becomes more top heavy, the number density of Pop III star-forming halos decreases, especially at $z < 12$. This can be explained by the more efficient enrichment of the IGM due to the higher number of energetic PISN supernova for the more top-heavy IMFs. In this work, the end of the Pop III era is driven by the external enrichment of low-mass halos and the IGM by enriched ejecta from Pop II star-forming halos. We discuss this in more detail in Section 3.2.

We now look at the case of a strong-LW background in more detail. The strong-LW background used here is that generated by the Trenti & Stiavelli (2009) model with massive Pop III stars forming with $\epsilon = 0.05$. This stronger background approximates the case of Pop III star formation near an overdense region or protocluster. Effectively, this strong-LW background suppresses all Pop III star formation in halos with $M_{\text{vir}} < M_{\text{HI}}$ in the following manner. Via dissociation of H_2 , the LW background suppresses Pop III star formation in halos with $M_{\text{vir}} < M_{\text{LW}}$ unless $M_{\text{vir}} > M_{\text{HI}}$. For a strong enough LW background, the redshift at which $M_{\text{LW}} = M_{\text{HI}}$ is approximately as high or higher than the redshift at which the first halos with

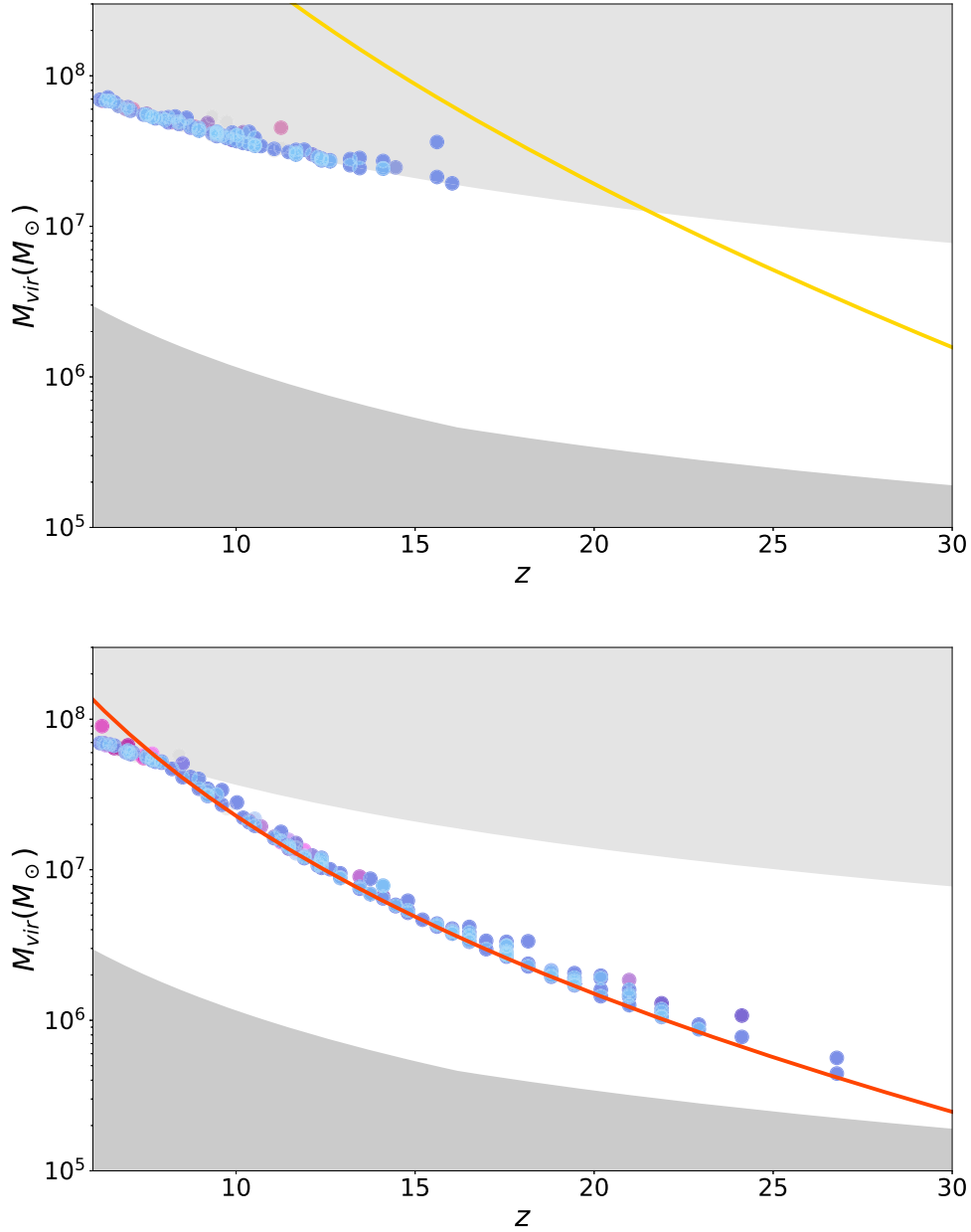


Figure 5. The virial mass vs. redshift for the halos hosting Pop III stars for strong (upper) and weak (lower) LW backgrounds. The dark gray shaded region is $M_{\text{vir}} < M_{\text{III}}(z)$, where no Pop III stars will form due to insufficient mass or coolant. The light gray shaded region is where $M_{\text{vir}} > M_{\text{HI}}$, where H I cooling and self-shielding of H_2 allow Pop III stars to form regardless of the strength of the LW background. Mass thresholds due to the weak (red) and strong (gold) LW backgrounds are shown by dotted lines. Each point is a halo and the colors correspond to the Pop III IMFs in Figure 2.

$M > M_{\text{HI}}$ collapse. As seen in the left panel of Figure 5, this not only delays the local onset of Pop III star formation to $z < 15$, but increases the typical halo masses by 2 orders of magnitude from $\approx 10^5\text{--}10^6 M_{\odot}$ to $\approx 10^7\text{--}10^8 M_{\odot}$.

The delay of Pop III star formation until $z < 15$ seen for our strong-LW background is similar to the Bowman et al. (2018) result placing the start of Pop III star formation at 17 ± 2 based on measurements of the width of the H II edge at 78 MHz.

We parameterize whether a given LW background is able to suppress Pop III star formation in all non-atomic-cooling halos with the relationship between two redshifts, z_{LW} and z_{HI} . The first, z_{LW} , is the redshift at which the mass threshold determined by the strength of the LW background, M_{LW} (Equation (3)), crosses the atomic cooling threshold. At

$z < z_{\text{LW}}$ the mass threshold that governs which halos are able to form Pop III stars is M_{HI} . The second redshift, z_{HI} , is the redshift at which the first halos in the simulation exceed the atomic cooling threshold. In our representative box, $z_{\text{HI}} \approx 15$. If $z_{\text{LW}} < z_{\text{HI}}$, then the LW background suppresses Pop III star formation in non-atomic-cooling halos, delaying the end of the dark ages. This effect mimics the delay in halo formation and suppression of low-mass halos in the warm dark matter model (WDM; Avila-Reese et al. 2001; Dayal et al. 2015). However, unlike the global effect of WDM, a delay in Pop III star formation due to a strong-LW background is a local effect: It will occur in regions which are far enough from early Pop III star formation sites to remain unenriched, yet close enough to be affected by the LW background they generate.

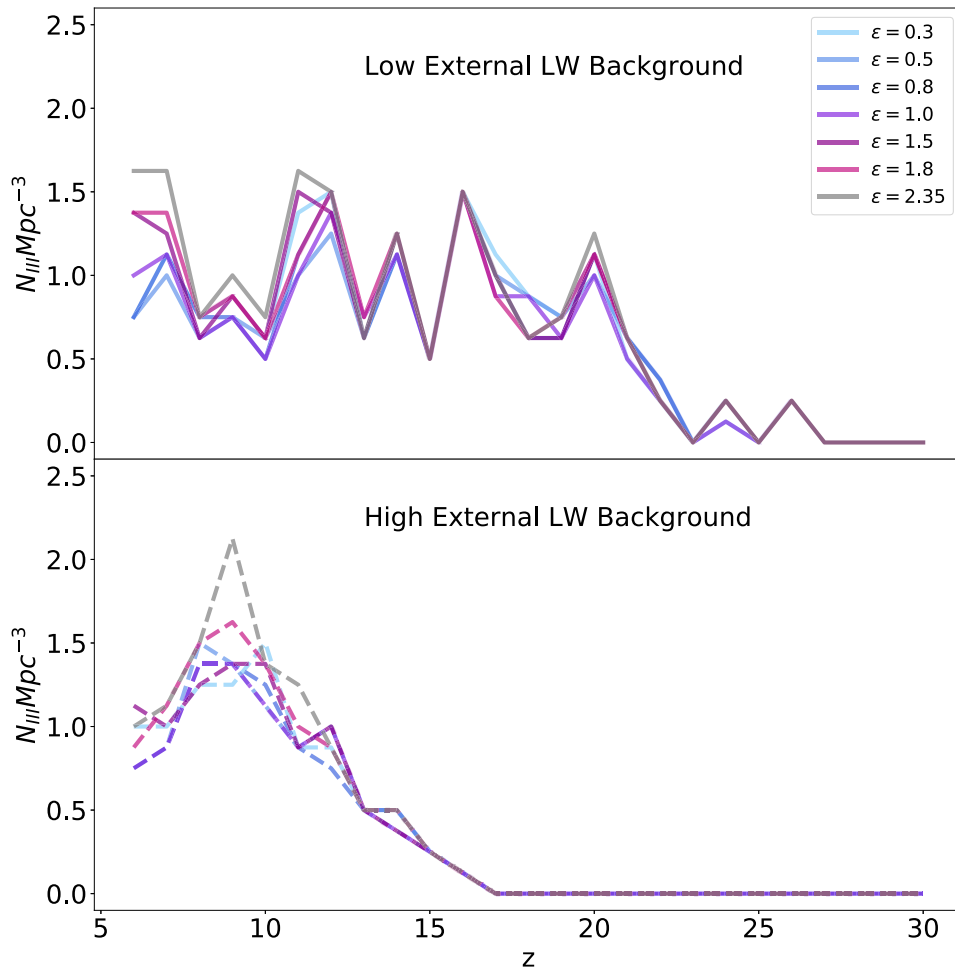


Figure 6. Number of Pop III star-forming halos per cubic megaparsec for a range of IMFs at a given redshift vs. redshift for a weak (upper) and strong (lower) external LW background. Colors of the various IMFs are the same as in Figure 2.

Differentiating between the two will require probing the redshifts of Pop III star formation along multiple sight lines, and in a large range of local environments.

3.2. Pop III Initial Mass Function

We now look in detail at what variations our model produces in the Pop III IMFs considered in this work. In Figures 5, 6, and 7 we assume fiducial values for the minimum and maximum masses of Pop III stars of $m_{\min} = 10 M_{\odot}$ and $m_{\max} = 1000 M_{\odot}$.

We first look at variations which are independent of the LW background. While the redshift at which Pop III stars begin to form is independent of the Pop III IMF, Figure 5 shows that there are subtle differences in which halos form Pop III stars for the different IMFs. These differences are highlighted in Figure 6, which shows the number density of Pop III star formation halos at $z < 6$. We find that, regardless of the strength of the LW background, the number of Pop III star-forming halos at a given redshift decreases as the IMF becomes more top heavy. We now explore the reason behind this trend.

To zeroth order, the number of PISNe will increase as the IMF becomes more top heavy. While the energy from CCSNe alone is capable of sending enriched ejecta into the IGM around the lowest-mass Pop III star-forming halos at $z > 20$, higher-mass Pop III star-forming halos at lower redshift require

the energy from at least one PISN in order to send enriched ejecta into the surrounding IGM. As the Pop III IMF becomes more top heavy, the number of PISNe increases and R_{ejecta} becomes larger, decreasing the number of halos at later redshifts which remain pristine.

This scenario also accounts for the larger differences in the number of Pop III star-forming halos seen in Figure 6. While a larger range of Pop III IMFs produce sufficiently energetic supernova ejecta to enrich nearby halos, only more top-heavy IMFs will be able to externally enrich the regions around the more massive Pop III star-forming halos forming in the presence of a stronger LW background.

The peaks and valleys seen in Figures 6 and 8 for all Pop III IMFs are an effect of LW background in our model. The first Pop III stars form, increasing the LW background, and suppressing Pop III star formation in the lower-mass halos, decreasing the number density of Pop III star-forming halos and the production of LW photons. Eventually, the original photons will be redshifted out of the LW bands, decreasing the local LW background and allowing Pop III stars to form in lower-mass halos again, increasing their number density. The location and relative heights of the peaks are dependent on the specific merger trees generated from the N -body simulation. However, not every portion of a JWST NIRCcam pointing will be at the same local density. To

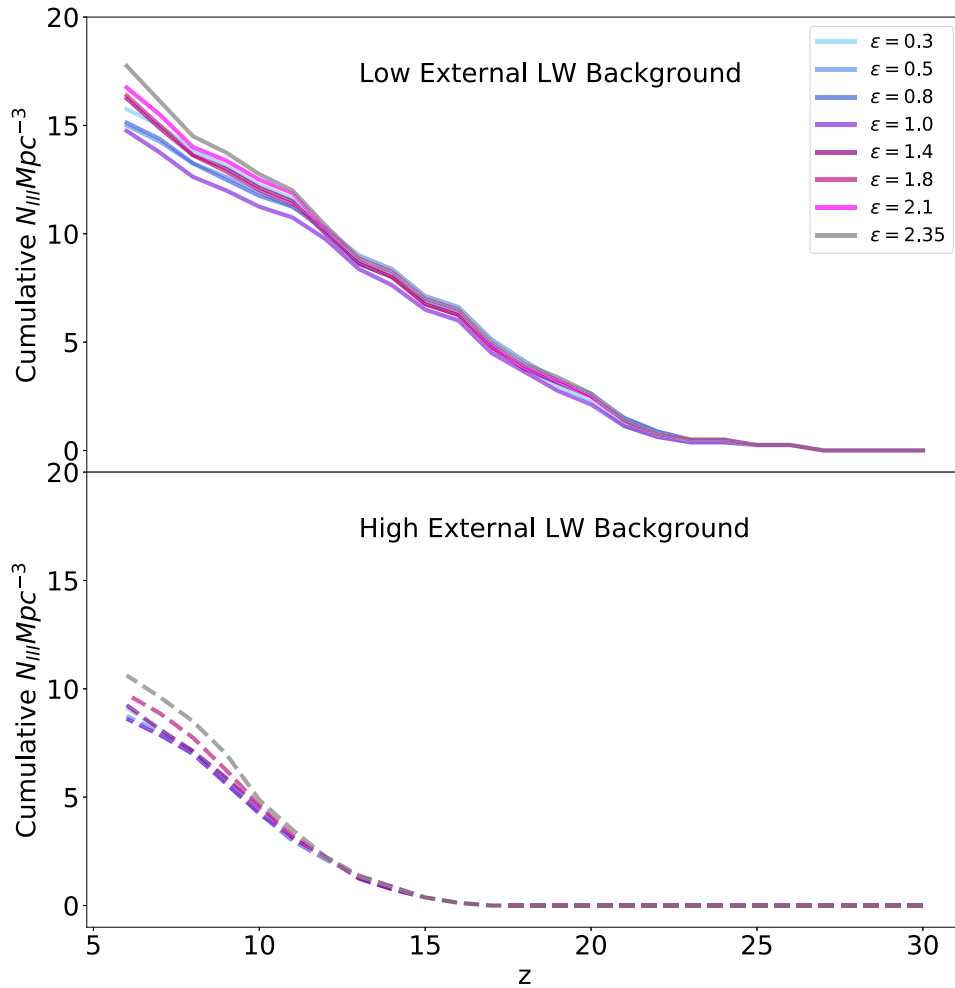


Figure 7. Cumulative number of Pop III star-forming halos per cubic megaparsec for a range of IMFs at a given redshift vs. redshift for a weak (upper) and strong (lower) external LW background. Colors of the various IMFs are the same as in Figure 2.

account for this, we assume regions of overdensities evolve faster and regions of underdensities evolve slower. To this end, we can average the number density of Pop III stars over a range of redshifts, which is expected to decrease the amplitude of the spikes.

3.3. Fraction of Supernovae in Mechanical Energy

In our enrichment model, the efficiency with which Pop III supernovae can enrich their host halos and the surrounding IGM is directly dependent on the amount of kinetic energy those supernovae inject into the enriched gas. As discussed in Section 2.1.4, the total energy generated by Pop III supernovae depends on the number of CCSNe and PISNe in a given halo. In our model, we assume a fraction of the total supernova energy, f_{kin} , goes into kinetic feedback, which drives the expansion of the enriched ejecta and the enrichment of the host halo and nearby halos. From literature on hydrodynamic simulations (Martizzi et al. 2015; Hopkins et al. 2018; Oku et al. 2022) and other modeling (Dalla Vecchia & Schaye 2008; Crain et al. 2015; Kim & Ostriker 2015; Keller et al. 2022), we have selected three representative values of $f_{\text{kin}} = 0.1$ – 1.0 with a fiducial value of $f_{\text{kin}} = 0.3$.

Figure 8 shows the dependence on the number density of Pop III stars on the choice of f_{kin} for two extrema of our Pop III IMFs, $\alpha = 0.2$ and $\alpha = 2.35$. As expected, we find that

increasing f_{kin} lowers the number density of Pop III star-forming halos at $z < 15$. We confirm previous results (Smith et al. 2015; Chen et al. 2017; Jaacks et al. 2018; Hicks et al. 2021) which show that the primary driver of the halo and IGM enrichment and the end of the Pop III era is not self-enrichment from Pop III star formation in a given halo, but external enrichment of nearby halos by enriched ejecta from Pop III supernovae. Therefore, increasing the amount of kinetic energy injected by Pop III supernovae will increase the range of the enriched ejecta and decrease the number of halos which retain their primordial composition.

As seen in Figure 8 and 9, changing f_{kin} for a given Pop III IMF produces a spread in the number density of Pop III stars which is greater than for various Pop III IMFs for a given f_{kin} . However, it is reasonable to assume that f_{kin} is relatively constant in Pop III star-forming halos, and the shifts are similar regardless of the chosen Pop III IMF.

4. Detectability with JWST

In Figure 10, we plot the magnitude of Pop III star clusters in the rest-frame 1400 Å band versus number density of Pop III sources per arcsec² for our various LW backgrounds (colors) and Pop III IMFs (shapes) for three JWST filters: F115W, F150W, and F200W. Since we can assume the spectral energy distribution of Pop III stars emits almost all of its light in the

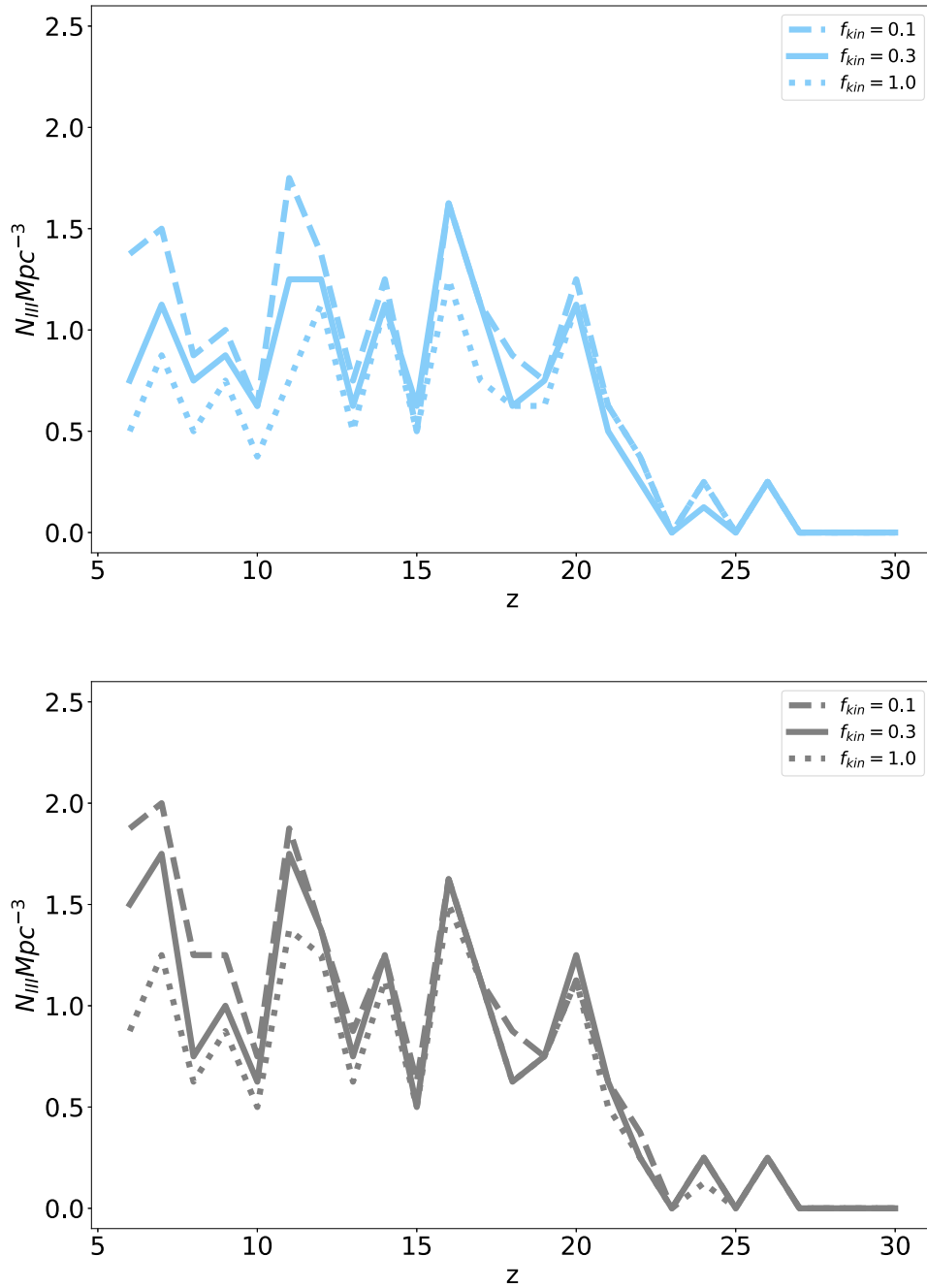


Figure 8. Number of Pop III star-forming halos per cubic megaparsec for three possible fractions of supernova energy which go into kinetic feedback, $f_{\text{kin}} = 0.1$ (dashed line), $f_{\text{kin}} = 0.3$ (solid line), and $f_{\text{kin}} = 1.0$ (dotted line) for $\alpha = -0.2$ (upper) and $\alpha = -2.35$ (lower). The range in the number density of Pop III stars vs. redshift for the fiducial value of f_{kin} are shown as the colored lines corresponding to the Pop III IMFs in Figure 2.

UV, each of these filters probes the Pop III population and LW background at a different redshift. Based on the center wavelengths, F115W probes $z = 8.4$, F150W probes $z = 10.4$, and F200W probes $z \approx 15$.

We find that our models occupy distinct space in the number density of Pop III sources on the sky versus magnitude space for the F115W, F150W, and F200W JWST filters. This shows that when the first Pop III stars are detected their number density and magnitudes will allow us to constrain the LW background at high redshift and/or the Pop III IMF, with a filter dependence on the effectiveness of the constraint. While

too faint for direct detection in even the deepest JWST fields, Pop III star clusters are bright enough to be seen with magnifications typically seen in the Frontier Fields (Zackrisson et al. 2015) and in the GLASS Early Release Science observations with JWST (Roberts-Borsani et al. 2022).

We find, regardless of the LW background and Pop III IMF, there are an order of 100–1000 Pop III star-forming halos per NIRCcam pointing in all three filters. In F115W, there are ~ 1000 Pop III star-forming halos per NIRCcam pointing for the low-LW background and ~ 1500 Pop III star-forming halos per NIRCcam pointing for our high-LW background.

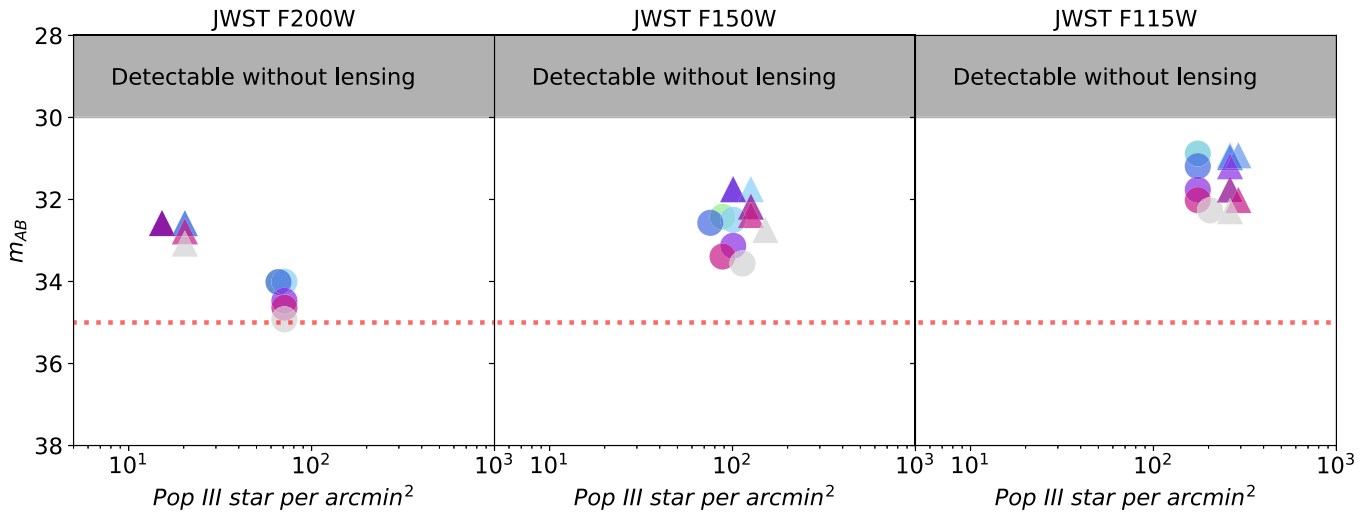


Figure 9. Apparent AB magnitude vs. number of Pop III star-forming halos per arcmin² assuming a maximum Pop III stellar mass of $1000 M_{\odot}$ for our range of Pop III IMF slopes (colors from Figure 2) and a weak (circles) and strong (triangles) external LW background. The shaded region shows magnitudes where a Pop III star cluster would be detectable by a deep NIRCам pointing (dark gray), and the maximum magnification from gravitational lensing typical of the Frontier Fields is denoted by the dotted red line. Pop III star clusters below this line are only detectable via rare caustic crossing events. We show the relation for three NIRCам filters corresponding to a $\Delta z \approx 1$ centered on $z = 15.4$ (left), $z = 11.3$ (center), and $z = 8.4$ (right).

In F150W, we find ~ 500 Pop III star-forming halos per NIRCам pointing for both LW background strengths, though in general the high-LW background produces a slightly higher number density of more luminous star-forming halos in the filter. This is expected given that at $z \sim 11$ the delay in Pop III star formation for the stronger LW background means Pop III stars will be forming in higher-mass pristine halos in greater number densities than for the lower-LW background where many of these atomic cooling halos are enriched.

It is in F200W, probing $z \sim 15$, where the strength of the LW background produces an order-of-magnitude difference in the number of Pop III star-forming halo per NIRCам pointing. While the low-LW background produces ~ 350 Pop III star-forming halos per NIRCам pointing, the suppression of star formation in low-mass halos by the high-LW background means that for the stronger LW background there are only ~ 50 Pop III star-forming halos per NIRCам pointing.

These results underscore the importance of observations across multiple filters in order to disentangle environmental effects like the LW background from the Pop III IMF in m_{AB} -number density space. A weaker LW background will produce a steady increase in both number density and magnitude from F200W to F115W. In contrast, the suppression of Pop III star formation in low-mass halos by a strong LW background produces a lesser increase in magnitude but an increase in number density of a factor of 20 across the same filters. How these trends translate to observations of magnified Pop III stars in the Frontier Fields will be the subject of an upcoming paper.

For all JWST filters, we find more top-heavy IMFs produce more luminous Pop III star-forming halos irrespective of the local LW background and the maximum mass of the Pop III IMF. This is a consequence of the consideration of both the Pop III star formation efficiency and the fragmentation limits of primordial gas in our model. As seen in Figure 4, the de facto Pop III star formation efficiency of Pop III star formation increases as the IMF becomes more top heavy.

For the more bottom-heavy IMFs, the total mass in Pop III stars is limited by the fragmentation of primordial gas, limiting their luminosities.

5. Conclusions

We have presented the initial results from a novel model of Pop III star formation which accounts for the limitations of the fragmentation of primordial gas while treating the Pop III IMF and maximum mass as truly free parameters. While relatively simple, our model is able to roughly reproduce the Pop III star formation rates seen in Skinner & Wise (2020) for an equivalent IMF. In this work, we use our model to explore Pop III star formation for a range of IMFs.

A critical component of our work is the inclusion of a model for the fragmentation of primordial gas based on simple assumptions for Jeans collapse in $>10^7 M_{\odot}$ halos. We find that the expected lower fragmentation of primordial gas limits the number of Pop III stars which can form, especially for the more bottom-heavy IMFs. Our results suggest that the shape of the Pop III IMF may be driven by the efficiency of the fragmentation of primordial gas. In halos where higher angular momentum and turbulence have driven additional fragmentation, the Pop III IMF may form Pop III stars of lower masses. The full implications of a potentially nonuniversal Pop III IMF and a more detailed study of how the efficiency of primordial gas fragmentation compares to our simple model for various halo mass and redshifts are both subjects for future study.

If direct detection is possible, the number density of Pop III stars at a given redshift in one NIRCам pointing is greater than 1, and greater than 10 for certain combinations of LW background and Pop III IMFs.

We find that, while the number density of Pop III stars is relatively independent of the mass distribution of Pop III stars, the magnitude of Pop III star clusters is 2–3 magnitudes higher for top-heavy Pop III IMFs than for their more bottom-heavy counterparts. In addition, this result is relatively independent of the assumption for the maximum mass of Pop III stars.

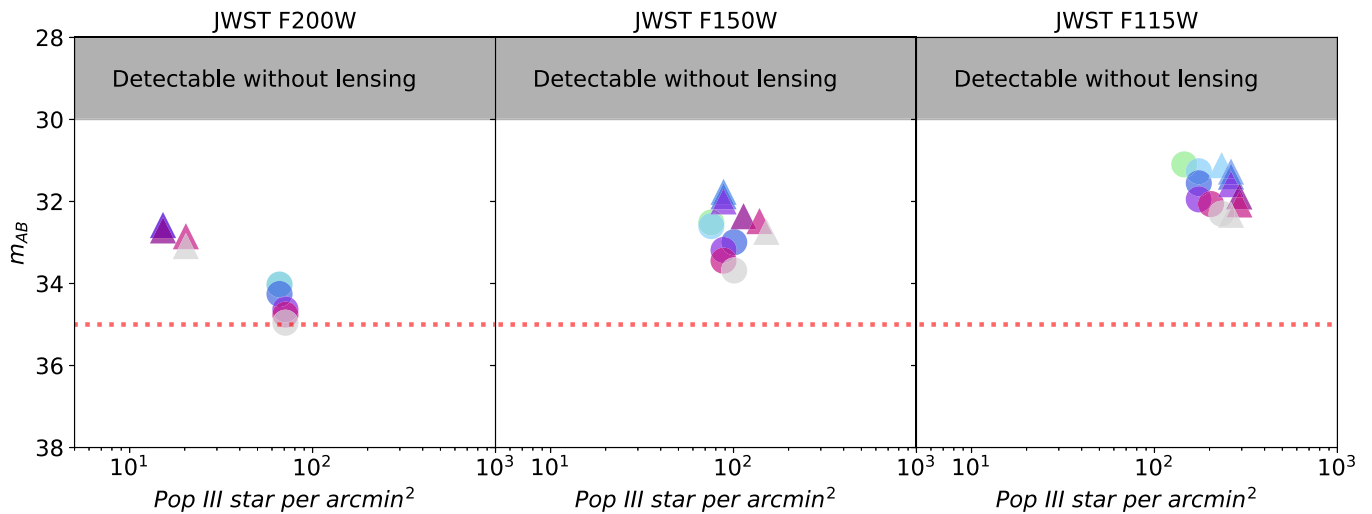


Figure 10. Apparent AB magnitude vs. number of Pop III star-forming halos per arcmin² assuming a maximum Pop III stellar mass of 300 M_{\odot} for our range of Pop III IMF slopes (colors from Figure 2) and a weak (circles) and strong (triangles) external LW background. The shaded region shows magnitudes where a Pop III star cluster would be detectable by a deep NIRCcam pointing (dark gray), and the maximum magnification from gravitational lensing typical of the Frontier Fields is denoted by the dotted red line. Pop III star clusters below this line are only detectable via rare caustic crossing events. We show the relation for three NIRCcam filters corresponding to a $\Delta z \approx 1$ centered on $z = 15.4$ (left), $z = 11.3$ (center), and $z = 8.4$ (right).

While we find that all Pop III stars are too faint for direct detection by JWST, they are bright enough to be detected with magnification possible in the Frontier Fields for all combinations of Pop III IMF and LW background explored in this study. A quantification of how the dependence of the magnitudes of Pop III clusters on the IMF will affect the detectability of the first stars in upcoming JWST observations of lensing clusters will be the subject of a future study.

Acknowledgments

The authors acknowledge the University of Maryland supercomputing resources (<http://hpcc.umd.edu>) made available for conducting the research reported in this paper. This work was supported by NASA through grant No. 80NSSC21K1294.

ORCID iDs

Massimo Stiavelli <https://orcid.org/0000-0001-9935-6047>
 Massimo Ricotti <https://orcid.org/0000-0003-4223-7324>
 Michele Trenti <https://orcid.org/0000-0001-9391-305X>

References

- Abel, T., Bryan, G. L., & Norman, M. L. 2000, *ApJ*, 540, 39
 Abel, T., Bryan, G. L., & Norman, M. L. 2002, *Sci*, 295, 93
 Avila-Reese, V., Colín, P., Valenzuela, O., D’Onghia, E., & Firmani, C. 2001, *ApJ*, 559, 516
 Behroozi, P. S., Wechsler, R. H., Wu, H.-Y., et al. 2013, *ApJ*, 763, 18
 Bennett, C. L., Larson, D., Weiland, J. L., et al. 2013, *ApJS*, 208, 20
 Bowman, J. D., Rogers, A. E. E., Monsalve, R. A., Mozdzen, T. J., & Mahesh, N. 2018, *Natur*, 555, 67
 Bromm, V., Coppi, P. S., & Larson, R. B. 1999, *ApJL*, 527, L5
 Chen, K.-J., Whalen, D. J., Wollenberg, K. M. J., Glover, S. C. O., & Klessen, R. S. 2017, *ApJ*, 844, 111
 Chiaki, G., & Wise, J. H. 2019, *MNRAS*, 482, 3933
 Clark, P. C., Glover, S. C. O., Klessen, R. S., & Bromm, V. 2011, *ApJ*, 727, 110
 Crain, R. A., Schaye, J., Bower, R. G., et al. 2015, *MNRAS*, 450, 1937
 Dalla Vecchia, C., & Schaye, J. 2008, *MNRAS*, 387, 1431
 Dayal, P., Mesinger, A., & Pacucci, F. 2015, *ApJ*, 806, 67
 Diego, J. M., Broadhurst, T., Wong, J., et al. 2016, *MNRAS*, 459, 3447
 Diego, J. M., Broadhurst, T., Zitrin, A., et al. 2015, *MNRAS*, 451, 3920
 Dutta, J., Sur, S., Stacy, A., & Bagla, J. S. 2020, *ApJ*, 901, 16
 Gill, S. P. D., Knebe, A., & Gibson, B. K. 2004, *MNRAS*, 351, 399
 Glover, S. C. O., & Brand, P. W. J. L. 2001, *MNRAS*, 321, 385
 Greif, T. H., Springel, V., White, S. D. M., et al. 2011, *ApJ*, 737, 75
 Haemmerlé, L., Klessen, R. S., Mayer, L., & Zwick, L. 2021, *A&A*, 652, L7
 Hahn, O., & Abel, T. 2011, *MNRAS*, 415, 2101
 Heger, A., Fryer, C. L., Woosley, S. E., Langer, N., & Hartmann, D. H. 2003, *ApJ*, 591, 288
 Hicks, W. M., Wells, A., Norman, M. L., et al. 2021, *ApJ*, 909, 70
 Hopkins, P. F., Wetzel, A., Kereš, D., et al. 2018, *MNRAS*, 477, 1578
 Jaacks, J., Thompson, R., Finkelstein, S. L., & Bromm, V. 2018, *MNRAS*, 475, 4396
 Jauzac, M., Jullo, E., Eckert, D., et al. 2015a, *MNRAS*, 446, 4132
 Jauzac, M., Richard, J., Jullo, E., et al. 2015b, *MNRAS*, 452, 1437
 Jeon, M., Bromm, V., Besla, G., Yoon, J., & Choi, Y. 2021, *MNRAS*, 502, 1
 Keller, B. W., Kruijssen, J. M. D., & Chevance, M. 2022, *MNRAS*, 514, 5355
 Kim, C.-G., & Ostriker, E. C. 2015, *ApJ*, 802, 99
 Knollmann, S. R., & Knebe, A. 2009, *ApJS*, 182, 608
 Lam, D., Broadhurst, T., Diego, J. M., et al. 2014, *ApJ*, 797, 98
 Latif, M. A., Whalen, D., & Khochfar, S. 2022, *ApJ*, 925, 28
 Lazar, A., & Bromm, V. 2022, *MNRAS*, 511, 2505
 Martizzi, D., Faucher-Giguère, C.-A., & Quataert, E. 2015, *MNRAS*, 450, 504
 Moriya, T. J., Quimby, R. M., & Robertson, B. E. 2022, *ApJ*, 925, 211
 Ohkubo, T., Nomoto, K., Umeda, H., Yoshida, N., & Tsuruta, S. 2009, *ApJ*, 706, 1184
 Oku, Y., Tomida, K., Nagamine, K., Shimizu, I., & Cen, R. 2022, *ApJS*, 262, 9
 Park, J., Ricotti, M., & Sugimura, K. 2021a, *MNRAS*, 508, 6176
 Park, J., Ricotti, M., & Sugimura, K. 2021b, *MNRAS*, 508, 6193
 Prole, L. R., Clark, P. C., Klessen, R. S., & Glover, S. C. O. 2022, *MNRAS*, 510, 4019
 Ricotti, M. 2016, *MNRAS*, 462, 601
 Ricotti, M., Gnedin, N. Y., & Shull, J. M. 2000, *ApJ*, 534, 41
 Roberts-Borsani, G., Morishita, T., Treu, T., et al. 2022, *ApJL*, 938, L13
 Rydberg, C.-E., Zackrisson, E., Lundqvist, P., & Scott, P. 2013, *MNRAS*, 429, 3658
 Sarmento, R., Scannapieco, E., & Pan, L. 2017, *ApJ*, 834, 23
 Skinner, D., & Wise, J. H. 2020, *MNRAS*, 492, 4386
 Smith, B. D., Wise, J. H., O’Shea, B. W., Norman, M. L., & Khochfar, S. 2015, *MNRAS*, 452, 2822
 Sobral, D., Matthee, J., Darvish, B., et al. 2015, *ApJ*, 808, 139
 Springel, V. 2005, *MNRAS*, 364, 1105
 Stacy, A., Bromm, V., & Lee, A. T. 2016, *MNRAS*, 462, 1307
 Stiavelli, M. 2009, *From First Light to Reionization: The End of the Dark Ages* (New York: Wiley)
 Suda, T., Saitoh, T. R., Moritani, Y., Matsumo, T., & Shigejima, T. 2021, *PASJ*, 73, 609
 Sugimura, K., Matsumoto, T., Hosokawa, T., Hirano, S., & Omukai, K. 2020, *ApJL*, 892, L14

- Susa, H. 2013, *ApJ*, 773, 185
- Susa, H., Hasegawa, K., & Tominaga, N. 2014, *ApJ*, 792, 32
- Tegmark, M., Silk, J., Rees, M. J., et al. 1997, *ApJ*, 474, 1
- Trenti, M., & Stiavelli, M. 2009, *ApJ*, 694, 879
- Vanzella, E., Meneghetti, M., Caminha, G. B., et al. 2020, *MNRAS*, 494, L81
- Welch, B., Coe, D., Diego, J. M., et al. 2022, *Natur*, 603, 815
- Whalen, D. J., Even, W., Frey, L. H., et al. 2013, *ApJ*, 777, 110
- Whalen, D. J., Smidt, J., Even, W., et al. 2014, *ApJ*, 781, 106
- Windhorst, R. A., Timmes, F. X., Wyithe, J. S. B., et al. 2018, *ApJS*, 234, 41
- Wise, J. H., Turk, M. J., Norman, M. L., & Abel, T. 2012, *ApJ*, 745, 50
- Wollenberg, K. M. J., Glover, S. C. O., Clark, P. C., & Klessen, R. S. 2020, *MNRAS*, 494, 1871
- Xu, H., Norman, M. L., O'Shea, B. W., & Wise, J. H. 2016, *ApJ*, 823, 140
- Yoshida, N., Omukai, K., Hernquist, L., & Abel, T. 2006, *ApJ*, 652, 6
- Zackrisson, E., González, J., Eriksson, S., et al. 2015, *MNRAS*, 449, 3057